Ion kinetics in a Hot Flow Anomaly: MMS Observations

Steven J Schwartz[1,2], Levon Avanov[3], Drew Turner[4], Hui Zhang[5], Imogen Gingell[1], Jonathan P Eastwood[1], Daniel J Gershman[3], Andreas Johlander[6], Christopher T Russell[7], James L Burch[8], John C Dorelli[3], Stefan Eriksson[2], Robert E Ergun[2], Stephen A Fuselier[8,9], Barbara L Giles[3], Katherine A Goodrich[2], Yuri V Khotyaintsev[6], Benoit Lavraud[10], Per-Arne Lindqvist[6], Mitsuo Oka[11], Tai D Phan[11], Robert J Strangeway[7], Karlheinz J Trattner[2], Roy B Torbert[12], Andris Vaivads[6], Hanying Wei[7], Frederick Wilder[2]

[1]Imperial College London, London SW7 2AZ, UK
[2]Laboratory for Atmospheric and Space Physics, University of Colorado, Boulder, Colorado 80303, USA
[3]NASA, Goddard Space Flight Center, Greenbelt, Maryland 20771, USA
[4]The Aerospace Corporation, Los Angeles, California, USA
[5]Geophysical Institute, University of Alaska Fairbanks, Fairbanks, Alaska, USA
[6]Swedish Institute of Space Physics (Uppsala), Uppsala, Sweden
[7]Earth Planetary and Space Sciences, University of California, Los Angeles, California 90095, USA
[8]Southwest Research Institute, San Antonio, Texas 78238, USA
[9]University of Texas at San Antonio, San Antonio, Texas 78249, USA
[10]Institut de Recherche en Astrophysique et Planétologie, CNRS, UPS, CNES, Université de Toulouse, 31028 Toulouse, France
[11]Space Sciences Laboratory, University of California, Berkeley, California 94720, USA
[12]University of New Hampshire, Durham, New Hampshire 03824, USA

October 10, 2018

Key Points:

- MMS observations reveal distinct ion velocity-space populations within a Hot Flow Anomaly (HFA)
- The HFA interior varies smoothly in density with a swept-up pressure excess toward the trailing edge
- The HFA interior displays coherent kinematic coupling between anti-sunward and sunward backstreaming ions

---

Corresponding author: Steven J. Schwartz, `steven.schwartz@lasp.colorado.edu`

Abstract
Hot Flow Anomalies (HFAs) are transients observed at planetary bow shocks, formed by the shock interaction with a convected interplanetary current sheet. The primary interpretation relies on reflected ions channeled upstream along the current sheet. The short duration of HFAs has made direct observations of this process difficult. We employ high resolution measurements by NASA's Magnetospheric Multiscale mission to probe the ion microphysics within a HFA. MMS data reveal a smoothly varying internal density and pressure, which increase toward the trailing edge of the HFA, sweeping up particles trapped within the current sheet. We find remnants of reflected or other backstreaming ions traveling along the current sheet, but most of these are not fast enough to out-run the incident current sheet convection. Despite the high level of internal turbulence, incident and backstreaming ions appear to couple gyro-kinetically in a coherent manner.

Plain Language Shock waves in space are responsible for energizing particles and diverting supersonic flows around planets and other obstacles. Explosive events known as Hot Flow Anomalies (HFAs) arise when a rapid change in the interplanetary magnetic field arrives at the bow shock formed by, e.g., the supersonic "solar wind" plasma flow from the Sun impinging on the Earth's magnetic environment. HFAs are known to produce impacts all the way to ground level, but the physics responsible for their formation occur too rapidly to be resolved by previous satellite missions. This paper employs NASA's fleet of four Magnetospheric Multiscale satellites to reveal for the first time clear, discreet populations of ions that interact coherently to produce the extreme heating and deflection. **End Plain Language**

1 Introduction

The bow shock formed by the impact of the super-magnetosonic solar wind upon the Earth's magnetosphere has been the primary research laboratory for shock waves in collisionless plasmas. In addition to slowing, deflecting and heating the incident flow, the shock contends with multiple particle species and plasma fluctuations, giving rise to non-thermal processes including: selective acceleration of particles to high energies, growth of instabilities and development of non-Maxwellian particle distributions. See Paschmann, Schwartz, Escoubet, and Haaland (2005), Tsurutani and Stone (1985) and Burgess and Scholer (2015).

The interplanetary magnetic field orientation plays a central role in bow shock physics. Under quasi-perpendicular geometries, in which the angle θ_{Bn} between the field and shock normal is $> 45°$, and Alfvén Mach numbers $\gtrsim 3$, quasi-perpendicular shocks are "super-critical." Some incident solar wind ions reflect and subsequently gyrate into the downstream region. This mechanism turns directed bulk flow energy into internal energy. Under quasi-parallel geometries ($\theta_{Bn} \lesssim 45°$) some particles can escape upstream forming an extended turbulent foreshock populated by suprathermal ions.

Hot Flow Anomalies (HFAs) are the result of interplanetary current sheets changing the field orientation over kinetic scales at the bow shock (Paschmann, Haerendel, Sckopke, Moebius, & Luehr, 1988; Schwartz, Chaloner, Hall, Christiansen, & Johnstone, 1985; Schwartz et al., 2000; Thomsen, Gosling, Bame, Quest, & Russell, 1988; Thomsen, Gosling, Fuselier, Bame, & Russell, 1986). They have hot interiors containing flow strongly deflected from the anti-sunward direction; the over-pressure causes HFA expansion, driving shocks at one or both edges. Burgess (1989) demonstrated a mechanism (Burgess & Schwartz, 1988) in which ions reflected under quasi-perpendicular conditions were channeled upstream by the changing geometry. This process involves interplanetary $-\mathbf{V} \times \mathbf{B}$ electric fields which point toward the current sheet on at least one side (Thomsen et al., 1993). Simulations (Burgess & Schwartz, 1988; Omidi & Sibeck, 2007) support this scenario although statistical studies (Wang, Zong, & Zhang, 2013; Zhao, Zhang, & Zong, 2017b) show that HFA-like signatures are found under wider conditions.

HFAs can have a significant impact on the magnetopause (Sibeck et al., 1999, 2000), producing disturbances throughout the magnetosphere to the ground (Eastwood et al., 2011, 2008; Hartinger, Turner, Plaschke, Angelopoulos, & Singer, 2013; Zhao, Zhang, & Zong, 2017a). They have been observed at the bow shocks of Mercury (Uritsky et al., 2014), Venus (G. Collinson et al., 2015; G. A. Collinson et al., 2014), Mars (G. A. Collinson et al., 2012), Jupiter (Valek et al., 2017) and Saturn (Masters et al., 2008, 2009). They are frequent (> 3 per day (Facskó et al., 2008; Facskó, Németh, Erdos, Kis, & Dandouras, 2009; Schwartz et al., 2000); ~ 7 can be observed within a 12 hour interval (Zhang et al., 2010)).

HFAs are typically a few minutes in duration. "Mature HFAs" have hot interior regions, with a single ion component and near-Maxwellian electron distributions (Thomsen et al., 1988). "Young HFAs" have central regions in which the solar wind beam is distinct from counter-streaming ions (Lucek, Horbury, Balogh, Dandouras, & Rème, 2004; Shestakov & Vaisberg, 2016; Zhang et al., 2010) which may be of magnetosheath origin (Vaisberg, Shuvalov, Shestakov, & Golubeva, 2016), although the central temperatures are often too high to be explained by a simple conversion of solar wind kinetic energy (Onsager, Thomsen, & Winske, 1990; Wang et al., 2013).

Recent work (Liu, Angelopoulos, & Hietala, 2017; Turner et al., 2018) explored the energetic particle populations at HFAs. Past work on HFA formation and heating mechanisms has utilized higher-resolution electromagnetic field data, with particle information accumulated over $\sim 3-4$ seconds. Consequently, many details, including proposed turbulent vs. coherent heating and energisation mechanisms, are not well resolved. We take advantage of the high resolution full 3D velocity-space particle data taken by NASA's Magnetospheric Multiscale Mission (MMS) (Burch, Moore, Torbert, & Giles, 2016) to study this microphysics.

2 Data

2.1 Instruments

We study a HFA that was captured in burst mode on 2015/12/28 at 05:27 UT. Fast Plasma Investigation (FPI) electron (ion) measurements have 30(150) ms cadences (Pollock et al., 2016). The excellent agreement of the electron and ion densities here suggests that the HFA interior is very well-characterized by the measurements, although FPI is not able to capture accurately the cold, low density solar wind plasma with the same accuracy (see Supplementary Information (SI)). Fields data (Torbert et al., 2016) including FGM magnetic field (Russell et al., 2016) at 128 vectors/second are used together with electric field measurements derived from the spin-plane (SDP (Lindqvist et al., 2016)) and axial (ADP (Ergun et al., 2016)) booms. The Hot Plasma Composition Analyzer (HPCA) (Young et al., 2016) provides alpha particle data.

2.2 Event overview

Figure 1 presents an overview of the HFA plasma and field data. The current sheet-bow shock intersection moves northward as it convects with the solar wind. The orientation of the leading (Earthward) edge at 05:26:52 UT is sketched in Figure 2. Figure 2b shows the high inclination of the current sheet, exaggerated by the inclination of the leading edge based on 4-spacecraft timing of the inner boundary (see $\mathbf{n}_{leading}$ in

Table 1), that results in a weak northward and anti-sunward compression (see Lucek et al. (2004) Figure 3) predominantly transverse to the Sun-Earth line.

The trailing edge shows a strong sunward magnetic compression (panel (d)) associated with a high Mach number shock (Fuselier, Thomsen, Gosling, Bame, & Russell, 1987). The compression magnitude is similar to the bow shock crossing two minutes later (SI Figure S2). The orientation of this edge (Figure 2b) is sunward and southward. It will relax to the nominal bow shock position as the current sheet-bow shock intersection tracks northward.

There is a clear pre- to post-HFA change in interplanetary field orientation (see Figure 2a and Table 1). The interior density depression (Figure 1f) is followed by a gradual rise toward the trailing edge compression. This depression, by an order of magnitude from solar wind values, is much greater than the relative magnetic field depression ~ 2.5. Thus, in addition to the 2D expansion transverse to $\mathbf{B}$ there must be some expansion, e.g., along the current sheet. The HFA interior is hot (panel (j)) and shows significant flow deflection (panel (h,i)), primarily in the $+z$ direction, consistent with the overall HFA motion, and deceleration in x.

Table 1 summarizes the HFA and solar wind conditions. The geometry of the bow shock and interplanetary current sheet control HFA formation and evolution (Paschmann et al., 1988; Schwartz et al., 1985; Schwartz, Kessel, Brown, Woolliscroft, & Dunlop, 1988; Thomsen et al., 1988). Figure 2a sketches the current sheet orientation based on the cross product between the pre- and post-HFA magnetic fields and assuming the sheet is a tangential discontinuity. Figure 2b shows the orientations of the leading and trailing edges.

Schwartz et al. (2000) introduced the ratio $|V_{tr}/V_g|$ between the velocity of the bow shock-current sheet intersection point and the gyro-velocity of a specularly reflected ion. Table 1 shows that this ratio is small enough to give ions reflected at the shock access to the current sheet before convection moves it too far along the shock. The orientation of the solar wind $-\mathbf{V}\times\mathbf{B}$ electric field points toward the current sheet on both sides, bringing bow shock reflected ions toward, rather than away from, the current sheet.

The leading and trailing edge speeds and orientations given in Table 1 were calculated based on four spacecraft timing analysis (e.g., Schwartz, 1998). Projecting the difference between these two edge velocities along the underlying current sheet normal provides an estimate of the HFA expansion speed of 68 km/s, similar to other reported values (Liu, Turner, Angelopoulos, & Omidi, 2016; Schwartz et al., 1985).

Table 1 also shows calculations of the HFA extent $\sim 2.3\ R_E$ along the bow shock. From the intersection of the two edges, the HFA projects $\sim 1\ R_E$ upstream. Table 1 calculates the HFA age and distance from its birth.

3 Results and Discussion

3.1 Ion kinetics - Early interior

Figure 3 (A-B) shows ion distributions observed at locations within the HFA, reduced by cartesian integration onto the plane containing the GSE X-axis and current sheet normal. This orientation matches qualitatively that of Figures 2(a,b). Panes (D-E) are similar integrations onto planes related to the magnetic field (see caption and axis labels). Pane A(a) shows the pre-event solar wind beam traveling at $V_x \approx -500$ km/s. The solar wind alpha particles appear as a second peak at $V_x \approx -650$ km/s. This region of velocity space is populated throughout much of the HFA. The white line in panes A(b,e) (omitted elsewhere for clarity) indicates velocities tangential to the current sheet in a frame convecting with it. Particles traveling upstream within the current sheet will lie near the sunward (right) portion of this line.

On HFA entry (Pane A(b)), peaks remain at the solar wind proton and alpha locations, reduced significantly in density. Pane A(b) shows an extended population with velocities along the convecting current sheet (along the white line). This extended population may originate from deeper in the HFA or magnetosheath (Vaisberg et al., 2016).

The solar wind beam persists through the first half of the HFA (row (A)) with only modest spreading and deflection. It is accompanied by three distinct groups of ions and a broader population (see numbers in Pane A(e)):

1. A low energy population toward the center of the panes (cf Pane A(d)), progressing from the white line to velocities with a component along the current sheet normal (Panes A(e,f)), i.e., southward and sunward relative to the convecting current sheet. This distinct group may have its origins in ions reflected by the bow shock and channeled along the current sheet as proposed by Burgess (1989).
2. A tight bunch traveling in the $+X_{GSE}$ direction with speeds $\sim 500 - 700\,\mathrm{km/s}$ most notable in Pane A(e). These may be newly reflected solar wind protons. From C(e) we see that these are close to the broader population discussed below occupying the lower portion of the skymap, most intense near $0^\circ/360^\circ$ azimuths. Panes (D-E)(e) reveal that these ions are not organized by the local magnetic field, consistent with their large gyroradii in the early portion of the HFA (see the third panel at the top).
3. A more dispersed sunward population with speeds comparable to the solar wind that peaks below the convection locus. This population is drifting toward the trailing edge of the HFA and may have been reflected earlier than group (2).
4. However, it is attached to a broader population that fills the upper portion of the panes, connecting smoothly onto the anti-sunward solar wind peak. From Pane D(e) we see that these ions, together with the remnant of the solar wind peak, are gyrating about the local magnetic field on the sunward and antisunward sides from the ion bulk velocity.

These distinct ion populations in the first half of the HFA are qualitatively consistent with our understanding of HFAs as kinetic phenomena. Collisionless, unmagnetized conditions preserve coherent phase-space features. It has not proven possible to link the individual features with sources before or after the intersection of the HFA leading edge with the nominal bow shock. The fall in density requires expansion (inferred from the wider perspective, see Table 1). Despite the apparent lack of coupling here, the fall in phase-space density requires dissipation.

Thus the first half of the HFA interior is characterized by phase-space clumps of ions including both the incident solar wind and, probably, relics of shock-reflected ions. Overall these features are distributed in the direction indicated by the white line (e.g., Pane A(b,e)), propagating upstream along and confined by the current sheet. However, they are moving sunward and southward with respect to that locus, and thus are unable to remain in step with the current sheet convection by the solar wind. This is consistent with the overall $V_z \sim +200\,\mathrm{km/s}$, less than the $470\,\mathrm{km/s}$ of V_{tr} (Table 1).

3.2 Ion kinetics - Late interior

The latter half of the HFA (Figure 3B) sweeps up particles unable to keep up with the current sheet convection. This region is denser with a stronger magnetic field, so that the gyroradius of a 1 keV proton, typical of the solar wind, falls below 1000 km, 1/7th of the HFA half-width. The more energetic protons fill the backstreaming hemisphere along the current sheet. This also corresponds to the post-HFA magnetic field direction (thin magenta line) in Figure 3C.

The solar wind peak bifurcates in Pane B(h) connected by a crescent around the magnetic field direction (Pane D(h)). Judging by its displacement from the origin (the center of momentum), it must be balanced in inertia by the more diffuse population in the right half corresponding to ions traveling along the current sheet in Figure 3B(h). Thus here there is sufficient backstreaming density to force the depleted solar wind peak into mutual gyration. There is also some relative field-aligned motion seen in E(h). This is evidence of a kinematic rather than turbulent coupling process, although the spread into a crescent may require some scattering in gyrophase.

There are still discreet features in the anti-sunward hemisphere from low to solar wind speeds. Two strong peaks appear in different orientations in Panes B(i) and (j). The larger of these is deflected southward, similar to that in the trailing edge compression region (Pane B(k)) which is the downstream "sheath" of the trailing shock. This flow drives the transverse expansion of the trailing edge. Pane D(i) shows that the smaller peak is gyrating around the larger one.

Finally, we note that the diffuse sunward-streaming population within the HFA is not organized by the local magnetic field, but in general fills the locus bounded by the post-HFA 90° pitch angle curve, cf., Pane C(i). While it is tempting to suggest that these ions have their source in the post-HFA quasi-parallel foreshock (Omidi & Sibeck, 2007), the post-HFA field-aligned backstreaming ions (e.g., C(l)) are far less intense than the ions found within the HFA. It is possible that they have the same or similar source, but that the interaction with the HFA, seen in the overall compression from leading to trailing edge, enhances their intensity. If so, they need to circumvent the trailing edge sheath, where their intensity is already close that seen in the post-HFA solar wind.

Thus the latter half of the HFA is characterized by an overall increase in ion density and a compactification of the phase space distribution. There remain distinct non-gyrotropic ion features that, in the larger magnetic fields found here, gyrate around their mutual center of momentum. This represents a coherent, kinematic coupling between the incident, anti-sunward ions and those backstreaming from the bow shock, magnetosheath or even internal HFA regions.

3.3 Alpha particles

The small, broken signal at twice the solar wind energy per charge seen pre- and post-HFA in Figure 1(a) are solar wind alphas. The HPCA instrument discriminates species and Figure 1(c) shows the alpha particle spectrogram. HPCA accumulates azimuths over a half spin (10 s). Thus the narrow solar wind alpha peak persists within the HFA interior as the small bright repeating feature, weakening in intensity within the HFA. It is accompanied by a more energetic alpha particle population that fills all azimuths (i.e., is present at all times) within the HFA, growing more intense toward the latter half of the HFA in common with the protons discussed above. Prior to entry into the trailing compression region, the alpha peak lowers in energy and is accompanied by a second narrow alpha population at even lower energies. As these two populations are observed at roughly the same time, they are at similar flow azimuths, corresponding to anti-sunward flow. They may contribute to the ions seen in Figure 3B(j). Together with the more diffuse alpha population this confirms that the solar wind alphas also participate in HFA dynamics and heating (Galvez, Fuselier, Gary, Thomsen, & Winske, 1990) evidenced by deceleration, bifurcation and diffuse components.

4 Summary

Using high resolution MMS observations, we probed ion kinetic signatures of a Hot Flow Anomaly. In the canonical HFA model (Burgess, 1989; Burgess & Schwartz, 1988; Omidi & Sibeck, 2007), the interaction of an interplanetary current sheet with the bow shock results, under suitable conditions, in reflected ions being channeled upstream along the current sheet where they couple with the solar wind beam. A resulting instability is then responsible for the strongly deflected, hot and nearly Maxwellian interior of "mature" HFAs (Thomsen et al., 1988; Zhang et al., 2010).

On the other hand, Vaisberg et al. (2016) studied a "young" HFA in which the solar wind beam is distinct. They suggested that the hot interior region in their event was the nominal magnetosheath plasma protruding into the upstream region.

The HFA studied here has not evolved into a nearly-Maxwellian state. The first half of the HFA retains a peak at the nominal solar wind ion energy, but reduced in density (and phase-space density) well below what would be expected from a 2D transverse expansion. We identified distinct groups of ions with velocities roughly aligned with the current sheet and propagating sunward with respect to the incident flow.

Deeper in the HFA, the solar wind component increases in density, while the backstreaming ions form distinct groups including both narrow sunward moving ions and broader backstreaming distributions unable to keep pace with the convecting current sheet. These particles drift toward the trailing edge of the HFA. We attribute the smooth increase in density throughout the HFA interior to such ions being swept up by the strongly compressed trailing edge.

The latter half of the HFA shows sufficient magnetic field compression to render ions of solar wind energies magnetized. However, the more diffuse, energetic backstreaming ions are not organized by the local magnetic field but instead fill a velocity-space hemisphere reminiscent of the current sheet and/or post-HFA interplanetary magnetic field. The dominant anti-sunward population is stretched into a velocity-space crescent, or appears as two distinct peaks. Analysis reveals that the different ion populations are in mutual gyration around their common center of momentum.

Thus, despite the presence of high amplitude bulk velocity fluctuations, this resolved gyration reveals a coherent coupling process between the incident and backstreaming ion populations. While we are not able to follow individual ions to their sources, the discreet, multi-component nature of the ion populations and their location in velocity space are consistent with the generic HFA theory of the channeling of reflected particles.

Some of the ion distributions are also reminiscent of contributions by pre-existing backstreaming ions (Vaisberg et al., 2016). Simulations (Omidi & Sibeck, 2007) suggest that in circumstances in which one side of the current sheet connects to the quasi-parallel bow shock, the HFA tends to form on that side. That is nearly the case here, although the post-HFA geometry is somewhat oblique ($\theta_{Bn} \sim 54^\circ$). While we have shown that that post-HFA field orientation is indeed consistent with the structure of the backstreaming diffuse population within the latter stages of the HFA, those ions are far more intense than the foreshock beam of ions found immediately on exiting the HFA.

5 Conclusions

We have explored kinetic aspects of the structure within a Hot Flow Anomaly observed near Earth's bow shock. The high-cadence MMS FPI plasma measurements reveal fine, unaliased signatures in ion velocity-space. Despite the high level of fluctuations, these signatures show a systematic evolution from one edge of the HFA to the other.

Unlike mature HFAs with hot near-Maxwellian cores, this HFA retains a peak in phase-space at/near the incident solar wind together with backstreaming clumps or diffuse ions which drift toward the HFA trailing edge. The incident and backstreaming populations couple kinematically through their mutual-gyration about the center of momentum rather than some more turbulent process.

Further work will explore the impact of solar wind alpha particles, which are shown here to display some of the same characteristics including a persistent diffuse backstreaming population and eventual deceleration/deflection. The electrons support large-amplitude fluctuations within the HFA (see SI); their kinetic characteristics are worthy of a separate investigation.

Table 1. Solar wind conditions & Current sheet/HFA parameters

Parameter	Value	Units
Spacecraft position	(11.1, -4.1, -1.1)	R_e (GSE)
Model bow shock normal[a]	(0.974, -0.219, -0.054)	GSE
β_i	2.3	<pre , post>$_{avg}$
V_{A,c_s}	21, 29	km/s <pre , post>$_{avg}$
M_{An} , M_{ms}	23, 14	shock Mach numbers <pre,post>$_{avg}$
Pre-event conditions	05:26:44.000-05:26:49.357	
$\mathbf{B}_{pre}$	(-0.824, -2.24, 0.708)	nT (GSE)
$\lvert\mathbf{B}_{pre}\rvert$	2.5	nT
$\theta_{Bn\ pre}$	98°(82°)	degrees
$n_{p\ pre}$ (WIND)	8.1	cm^{-3}
$\mathbf{V}_{pre}$ (WIND)	(-481, 12, -12)	km/s (GSE)
$T_{p\ pre}$ (WIND)	4	eV
$\mathbf{E}_{pre} = -\mathbf{V} \times \mathbf{B}$	(19, -350, -1100)	μV/m (GSE)
Post-event conditions	05:27:39.712–05:27:43.608	
$\mathbf{B}_{post}$	(1.95, 1.17, 1.38)	nT (GSE)
$\lvert\mathbf{B}_{post}\rvert$	2.7	nT
$\theta_{Bn\ post}$	54°	degrees
$n_{p\ post}$ (WIND)	6	cm^{-3}
$\mathbf{V}_{post}$ (WIND)	(-495, 3, -18)	km/s (GSE)
$T_{p\ post}$ (WIND)	6	eV
$\mathbf{E}_{post} = -\mathbf{V} \times \mathbf{B}$	(-30, -650, 600)	μV/m (GSE)
Current sheet/HFA parameters		
Current sheet normal, $\mathbf{n}_{cs}$	(0.680, -0.437, -0.590)	GSE ($\mathbf{B}_{post} \times \mathbf{B}_{pre}$)
$V_{ncs} \equiv \mathbf{V}_{sw} \cdot \mathbf{n}_{cs}$	-325	km/s
$\theta_{BpreBpost}$	120°	deg (magnetic shear angle)
$\mathbf{E}_{pre} \cdot \mathbf{n}_{cs}$	+810	μV/m (⇒ toward CS)
$\mathbf{E}_{post} \cdot \mathbf{n}_{cs}$	-80	μV/m (⇒ toward CS)
$\mathbf{n}_{leading}$	(-0.340, 0.633, 0.696)	4SC timing (inner edge)
$\mathbf{n}_{trailing}$	(0.861, 0.007, -0.508)	4SC timing (trailing shock)
$V_{n\ leading}$	234	km/s (4SC timing)
$V_{n\ trailing}$	-166	km/s (4SC timing)
$\Delta\mathbf{V}(trailing - leading) \cdot \mathbf{n}_{cs}$	68	km/s (HFA expansion)
$\theta_{Bn\ trailing}$	68°	degrees
$\mathbf{V}_{tr}$[b]	(77, 228, 473)	GSE km/s (CS track along shock)
$\lvert\mathbf{V}_{tr}/V_g\rvert_{pre\ ,\ post}$	0.6 , 0.7	ratio transit speed to gyration
Size ($V_{tr}\times$ 28s duration)	2.3	R_E
Extent upstream	1.0	R_E (to leading/trailing intersection)
Age	218	s (size/expansion speed)
Distance from birth	< 18	R_E (age $\times\lvert\mathbf{V}_{tr}\rvert$)

[a] Uses dayside empirical fit by Slavin and Holzer (1981). See also Schwartz (1998).

[b] Schwartz et al. (2000)

Figure 1. MMS1 overview of the HFA. (a) ion and (b) electron omni-directional differential energy fluxes [keV/(cm^2 s sr keV)] over-plotted with spacecraft potential (black line), (c) alpha particle flux [1/(cm^2 s sr eV)], (d) magnetic field strength and (e) GSE components, (f) electron and ion number densities, (g) bulk speeds and (h,i) GSE flow components, (j) electron and ion temperatures parallel and perpendicular to **B** and (k) thermal, magnetic and total pressures and ρV_x^2 ram pressure. Due to instrumental limitations in the solar wind (see SI), the thermal pressures shown in panel (k) are unreliable in the solar wind before and after the HFA; see values from the WIND spacecraft in Table 1. Dashed vertical lines denote the leading inner edge, trailing inner edge and trailing compression.

Figure 2. (a) Sketch of the bow shock–interplanetary current sheet interaction. Arrows show the solar wind magnetic field directions on either side. (b) 2-D schematic of the intersection of the interplanetary current sheet with the bow shock showing the approximate orientations of the leading and trailing edges. The structure appears to transit along the shock front at $\mathbf{V}_{tr}$ due to the convection of the current sheet by the incoming solar wind. Table 1 estimates the HFA size as $2.3\,R_E$ along the shock and $1\,R_E$ sunward from the nominal shock surface.

Figure 3. MMS1 reduced ion distributions. (Top) omni-directional spectrograms, magnetic field magnitude, gyroradii of protons in the local, 2.5 sec smoothed magnetic field. The dashed line is the HFA half-thickness. (A-B) FPI phase space distributions reduced by cartesian integration onto the X_{GSE}– (horizontal) current sheet normal (black arrow) plane. The circled dot and cross show the out-of-plane magnetic field component pre- and post-HFA. Letters correspond to times of each distribution indicated above the time series panel. The white circle locates the solar wind bulk velocity. The white line in panes A(b,e) are velocities with zero component along the current sheet normal in a frame convecting with the current sheet. (C) Polar vs. azimuthal angle skymaps. The thick magenta line represents 90° pitch angles in the spacecraft frame based on the local magnetic field direction, with a star indicating the tip of the field vector. The thin magenta line is the same but based on the post-HFA field direction. (D-E) Reduced distributions shifted to their bulk velocity frame and integrated onto the (D) $v_\perp - v_\perp$ and (E) $v_\perp - v_\parallel$ planes.

References

Burch, J. L., Moore, T. E., Torbert, R. B., & Giles, B. L. (2016, March). Magnetospheric Multiscale Overview and Science Objectives. *Space Sci. Rev.*, *199*, 5-21. doi: 10.1007/s11214-015-0164-9

Burgess, D. (1989, January). On the effect of a tangential discontinuity on ions specularly reflected at an oblique shock. *J. Geophys. Res.*, *94*, 472-478. doi: 10.1029/JA094iA01p00472

Burgess, D., & Scholer, M. (2015). *Collisionless shocks in space plasmas: structure and accelerated particles.* Cambridge University Press.

Burgess, D., & Schwartz, S. J. (1988, October). Colliding plasma structures - Current sheet and perpendicular shock. *J. Geophys. Res.*, *93*, 11327-11340. doi: 10.1029/JA093iA10p11327

Collinson, G., Halekas, J., Grebowsky, J., Connerney, J., Mitchell, D., Espley, J., . . . Jakosky, B. (2015, November). A hot flow anomaly at Mars. *Geophys. Res. Lett.*, *42*, 9121-9127. doi: 10.1002/2015GL065079

Collinson, G. A., Sibeck, D. G., Masters, A., Shane, N., Slavin, J. A., Coates, A. J., . . . Barabash, S. (2012, April). Hot flow anomalies at Venus. *J. Geophys. Res.*, *117*, A04204. doi: 10.1029/2011JA017277

Collinson, G. A., Sibeck, D. G., Masters, A., Shane, N., Zhang, T. L., Fedorov, A., . . . Sarantos, M. (2014, February). A survey of hot flow anomalies at Venus. *J. Geophys. Res.*, *119*, 978-991. doi: 10.1002/2013JA018863

Dunlop, M. W., & Woodward, T. I. (1998). Multi-Spacecraft Discontinuity Analysis: Orientation and Motion. *ISSI Scientific Reports Series*, *1*, 271-306.

Eastwood, J. P., Schwartz, S. J., Horbury, T. S., Carr, C. M., Glassmeier, K.-H., Richter, I., . . . Wild, J. A. (2011, August). Transient Pc3 wave activity generated by a hot flow anomaly: Cluster, Rosetta, and ground-based observations. *J. Geophys. Res.*, *116*, A08224. doi: 10.1029/2011JA016467

Eastwood, J. P., Sibeck, D. G., Angelopoulos, V., Phan, T. D., Bale, S. D., McFadden, J. P., . . . Le Contel, O. (2008, April). THEMIS observations of a hot flow anomaly: Solar wind, magnetosheath, and ground-based measurements. *Geophys. Res. Lett.*, *35*, L17S03. doi: 10.1029/2008GL033475

Ergun, R. E., Tucker, S., Westfall, J., Goodrich, K. A., Malaspina, D. M., Summers, D., . . . Cully, C. M. (2016, March). The Axial Double Probe and Fields Signal Processing for the MMS Mission. *Space Sci. Rev.*, *199*, 167-188. doi: 10.1007/s11214-014-0115-x

Facskó, G., Kecskeméty, K., Erdős, G., Tátrallyay, M., Daly, P. W., & Dandouras, I. (2008). A statistical study of hot flow anomalies using Cluster data. *Adv. Space Res.*, *41*, 1286-1291. doi: 10.1016/j.asr.2008.02.005

Facskó, G., Németh, Z., Erdos, G., Kis, A., & Dandouras, I. (2009, May). A global study of hot flow anomalies using Cluster multi-spacecraft measurements. *Ann. Geophys.*, *27*, 2057-2076. doi: 10.5194/angeo-27-2057-2009

Fazakerley, A. N., Schwartz, S. J., & Paschmann, G. (1998). Measurement of Plasma Velocity Distributions. *ISSI Scientific Reports Series*, *1*, 91-124.

Fuselier, S. A., Thomsen, M. F., Gosling, J. T., Bame, S. J., & Russell, C. T. (1987, April). Fast shocks at the edges of hot diamagnetic cavities upstream from the earth's bow shock. *J. Geophys. Res.*, *92*, 3187-3194. doi: 10.1029/JA092iA04p03187

Galvez, M., Fuselier, S. A., Gary, S. P., Thomsen, M. F., & Winske, D. (1990, August). Alpha particle heating in hot diamagnetic cavities. *J. Geophys. Res.*, *95*, 11975-11982. doi: 10.1029/JA095iA08p11975

Gershman, D. J., Avanov, L. A., Boardsen, S. A., Dorelli, J. C., Gliese, U., Barrie, A. C., . . . Pollock, C. J. (2017). Spacecraft and instrument photoelectrons measured by the dual electron spectrometers on MMS. *Journal of Geophysical Research: Space Physics*. doi: 10.1002/2017JA024518

Hartinger, M. D., Turner, D. L., Plaschke, F., Angelopoulos, V., & Singer, H.

(2013). The role of transient ion foreshock phenomena in driving pc5 ulf wave activity. *Journal of Geophysical Research: Space Physics*, *118*(1), 299–312. doi: 10.1029/2012JA018349

Kovács, P., Facskó, G., & Dandouras, I. (2014, March). Turbulent dynamics inside the cavity of hot flow anomaly. *Planet. Space Sci.*, *92*, 24-33. doi: 10.1016/j.pss.2014.01.001

Lin, R. P., Anderson, K. A., Ashford, S., Carlson, C., Curtis, D., Ergun, R., … Paschmann, G. (1995, February). A Three-Dimensional Plasma and Energetic Particle Investigation for the Wind Spacecraft. *Space Sci. Rev.*, *71*, 125-153. doi: 10.1007/BF00751328

Lindqvist, P.-A., Olsson, G., Torbert, R. B., King, B., Granoff, M., Rau, D., … Tucker, S. (2016, March). The Spin-Plane Double Probe Electric Field Instrument for MMS. *Space Sci. Rev.*, *199*, 137-165. doi: 10.1007/s11214-014-0116-9

Liu, T. Z., Angelopoulos, V., & Hietala, H. (2017). Energetic ion leakage from foreshock transient cores. *J. Geophys. Res.*, *122*(7), 7209–7225. (2017JA024257) doi: 10.1002/2017JA024257

Liu, T. Z., Turner, D. L., Angelopoulos, V., & Omidi, N. (2016, June). Multipoint observations of the structure and evolution of foreshock bubbles and their relation to hot flow anomalies. *J. Geophys. Res.*, *121*, 5489-5509. doi: 10.1002/2016JA022461

Lucek, E. A., Horbury, T. S., Balogh, A., Dandouras, I., & Rème, H. (2004, June). Cluster observations of hot flow anomalies. *J. Geophys. Res.*, *109*, A06207. doi: 10.1029/2003JA010016

Masters, A., Arridge, C. S., Dougherty, M. K., Bertucci, C., Billingham, L., Schwartz, S. J., … Thomsen, M. F. (2008, January). Cassini encounters with hot flow anomaly-like phenomena at Saturn's bow shock. *Geophys. Res. Lett.*, *35*, L02202. doi: 10.1029/2007GL032371

Masters, A., McAndrews, H. J., Steinberg, J. T., Thomsen, M. F., Arridge, C. S., Dougherty, M. K., … Coates, A. J. (2009, August). Hot flow anomalies at Saturn's bow shock. *J. Geophys. Res.*, *114*, A08217. doi: 10.1029/2009JA014112

Omidi, N., & Sibeck, D. G. (2007, January). Formation of hot flow anomalies and solitary shocks. *J. Geophys. Res.*, *112*, A01203. doi: 10.1029/2006JA011663

Onsager, T. G., Thomsen, M. F., & Winske, D. (1990, September). Hot flow anomaly formation by magnetic deflection. *Geophys. Res. Lett.*, *17*, 1621-1624. doi: 10.1029/GL017i010p01621

Paschmann, G., Haerendel, G., Sckopke, N., Moebius, E., & Luehr, H. (1988, October). Three-dimensional plasma structures with anomalous flow directions near the earth's bow shock. *J. Geophys. Res.*, *93*, 11279-11294. doi: 10.1029/JA093iA10p11279

Paschmann, G., Schwartz, S., Escoubet, C., & Haaland, S. (2005). *Outer magnetospheric boundaries: Cluster results* (No. 1-4). Springer Science & Business Media.

Pollock, C., Moore, T., Jacques, A., Burch, J., Gliese, U., Saito, Y., … others (2016, March). Fast Plasma Investigation for Magnetospheric Multiscale. *Space Sci. Rev.*, *199*, 331-406. doi: 10.1007/s11214-016-0245-4

Russell, C. T., Anderson, B. J., Baumjohann, W., Bromund, K. R., Dearborn, D., Fischer, D., … Richter, I. (2016, March). The Magnetospheric Multiscale Magnetometers. *Space Sci. Rev.*, *199*, 189-256. doi: 10.1007/s11214-014-0057-3

Schwartz, S. J. (1998). Shock and Discontinuity Normals, Mach Numbers, and Related Parameters. *ISSI Scientific Reports Series*, *1*, 249-270.

Schwartz, S. J., Chaloner, C. P., Hall, D. S., Christiansen, P. J., & Johnstone, A. D. (1985, November). An active current sheet in the solar wind. *Nature*, *318*, 269-271. doi: 10.1038/318269a0

Schwartz, S. J., Kessel, R. L., Brown, C. C., Woolliscroft, L. J. C., & Dunlop, M. W. (1988, October). Active current sheets near the earth's bow shock. *J. Geophys. Res.*, *93*, 11295-11310. doi: 10.1029/JA093iA10p11295

Schwartz, S. J., Paschmann, G., Sckopke, N., Bauer, T. M., Dunlop, M., Fazakerley, A. N., & Thomsen, M. F. (2000, June). Conditions for the formation of hot flow anomalies at Earth's bow shock. *J. Geophys. Res.*, *105*, 12639-12650. doi: 10.1029/1999JA000320

Shestakov, A. Y., & Vaisberg, O. L. (2016, March). Study and comparison of the parameters of five hot flow anomalies at a bow shock front. *Cosmic Res.*, *54*, 77-95. doi: 10.1134/S0010952516020064

Sibeck, D. G., Borodkova, N. L., Schwartz, S. J., Owen, C. J., Kessel, R., Kokubun, S., ... Zastenker, G. N. (1999, March). Comprehensive study of the magnetospheric response to a hot flow anomaly. *J. Geophys. Res.*, *104*, 4577-4594. doi: 10.1029/1998JA900021

Sibeck, D. G., Kudela, K., Lepping, R. P., Lin, R., Nemecek, Z., Nozdrachev, M. N., ... Yermolaev, Y. (2000, November). Magnetopause motion driven by interplanetary magnetic field variations. *J. Geophys. Res.*, *105*, 25155-25170. doi: 10.1029/2000JA900109

Slavin, J. A., & Holzer, R. E. (1981, December). Solar wind flow about the terrestrial planets. I - Modeling bow shock position and shape. *J. Geophys. Res.*, *86*, 11401-11418. doi: 10.1029/JA086iA13p11401

Thomsen, M. F., Gosling, J. T., Bame, S. J., Quest, K. B., & Russell, C. T. (1988, October). On the origin of hot diamagnetic cavities near the earth's bow shock. *J. Geophys. Res.*, *93*, 11311-11325. doi: 10.1029/JA093iA10p11311

Thomsen, M. F., Gosling, J. T., Fuselier, S. A., Bame, S. J., & Russell, C. T. (1986, March). Hot, diamagnetic cavities upstream from the earth's bow shock. *J. Geophys. Res.*, *91*, 2961-2973. doi: 10.1029/JA091iA03p02961

Thomsen, M. F., Thomas, V. A., Winske, D., Gosling, J. T., Farris, M. H., & Russell, C. T. (1993, September). Observational test of hot flow anomaly formation by the interaction of a magnetic discontinuity with the bow shock. *J. Geophys. Res.*, *98*, 15. doi: 10.1029/93JA00792

Torbert, R. B., Russell, C. T., Magnes, W., Ergun, R. E., Lindqvist, P.-A., LeContel, O., ... Lappalainen, K. (2016, March). The FIELDS Instrument Suite on MMS: Scientific Objectives, Measurements, and Data Products. *Space Sci. Rev.*, *199*, 105-135. doi: 10.1007/s11214-014-0109-8

Tsurutani, B. T., & Stone, R. G. (1985). *Collisionless shocks in the heliosphere: Reviews of current research* (Vol. 35). American Geophysical Union. doi: 10.1029/GM035

Turner, D. L., Wilson, L. B., Liu, T. Z., Cohen, I. J., Schwartz, S. J., Osmane, A., ... Burch, J. L. (2018, September). Autogenous and efficient acceleration of energetic ions upstream of earths bow shock. *Nature*, *561*(7722), 206–210. Retrieved from `https://doi.org/10.1038/s41586-018-0472-9`

Uritsky, V. M., Slavin, J. A., Boardsen, S. A., Sundberg, T., Raines, J. M., Gershman, D. J., ... Korth, H. (2014, February). Active current sheets and candidate hot flow anomalies upstream of Mercury's bow shock. *J. Geophys. Res.*, *119*, 853-876. doi: 10.1002/2013JA019052

Vaisberg, O. L., Shuvalov, S. D., Shestakov, A. Y., & Golubeva, Y. M. (2016, October). Origin of the backstreaming ions in a young Hot Flow Anomaly. *Planet. Space Sci.*, *131*, 102-110. doi: 10.1016/j.pss.2016.08.003

Valek, P. W., Thomsen, M. F., Allegrini, F., Bagenal, F., Bolton, S., Connerney, J., ... Wilson, R. J. (2017). Hot flow anomaly observed at jupiter's bow shock. *Geophysical Research Letters*, *44*(16), 8107–8112. doi: 10.1002/2017GL073175

Wang, S., Zong, Q., & Zhang, H. (2013, July). Hot flow anomaly formation and evolution: Cluster observations. *J. Geophys. Res.*, *118*, 4360-4380. doi: 10.1002/jgra.50424

Young, D. T., Burch, J. L., Gomez, R. G., De Los Santos, A., Miller, G. P., Wilson, P., … Webster, J. M. (2016, March). Hot Plasma Composition Analyzer for the Magnetospheric Multiscale Mission. *Space Sci. Rev.*, *199*, 407-470. doi: 10.1007/s11214-014-0119-6

Zhang, H., Sibeck, D. G., Zong, Q.-G., Gary, S. P., McFadden, J. P., Larson, D., … Angelopoulos, V. (2010, December). Time History of Events and Macroscale Interactions during Substorms observations of a series of hot flow anomaly events. *J. Geophys. Res.*, *115*(A14), A12235. doi: 10.1029/2009JA015180

Zhao, L. L., Zhang, H., & Zong, Q. G. (2017a, June). Global ULF waves generated by a hot flow anomaly. *Geophysical Research Letters*, *44*, 5283-5291. doi: 10.1002/2017GL073249

Zhao, L. L., Zhang, H., & Zong, Q.-G. (2017b, January). A statistical study on hot flow anomaly current sheets. *J. Geophys. Res.*, *122*, 235-248. doi: 10.1002/2016JA023319

Acknowledgments

SJS held a Leverhulme Research Fellowship hosted by LASP. We note with sadness the death of our colleague, Jack Gosling, who was involved in the early stages of the manuscript. MMS is a NASA-funded mission. MMS data is publicly available at the Science Data Center (https://lasp.colorado.edu/mms/sdc/public/). WIND data were drawn from CDAWeb (cdaweb.sci.gsfc.nasa.gov) and provided by A. Szabo, R. Lin, S. Bale and K. Ogilvie. Partial support included: UK/STFC grant ST/N000692/1 (SJS,JPE); NSF AGS-1352669 (HZ).

Figure 1

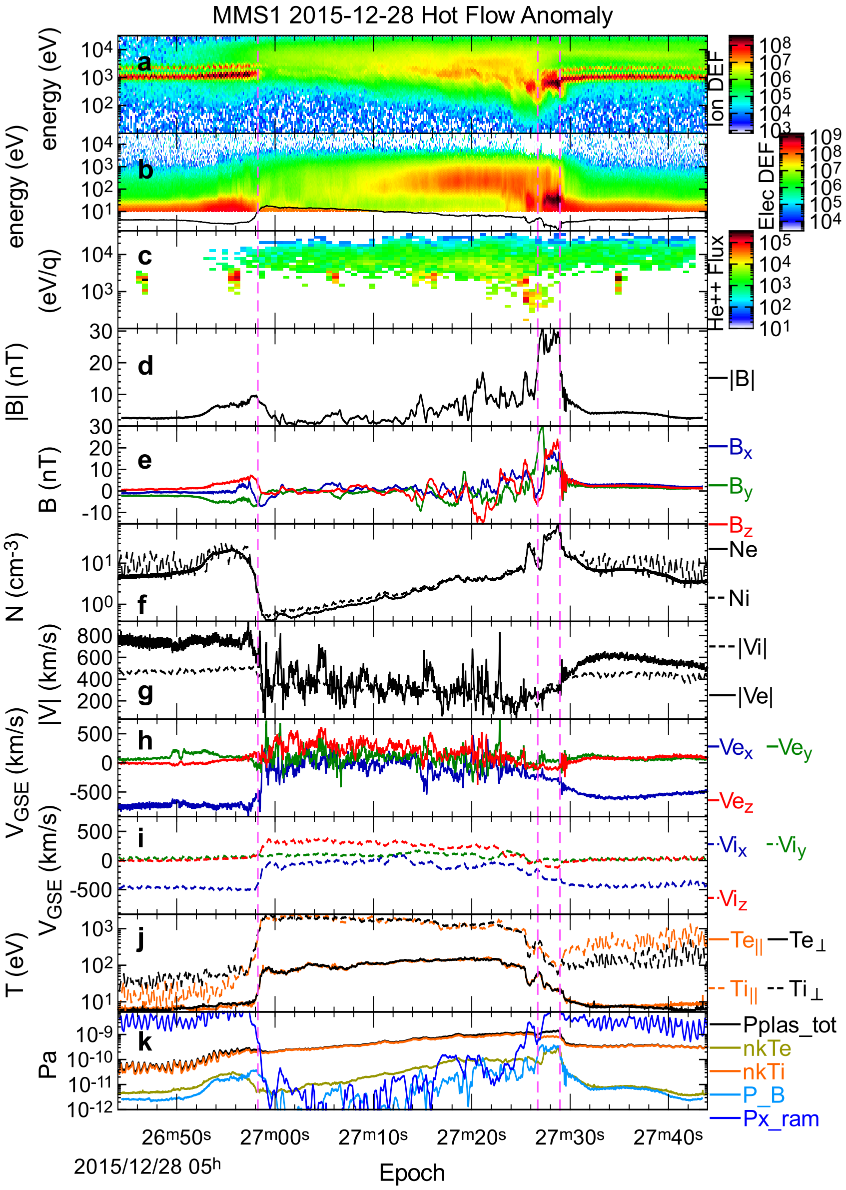
MMS1 2015-12-28 Hot Flow Anomaly
a
energy (eV)
Ion DEF
b
energy (eV)
Elec DEF
c
(eV/q)
He++ Flux
d
|B| (nT)
|B|
e
B (nT)
Bx
By
Bz
f
N (cm-3)
Ne
Ni
g
|V| (km/s)
|Vi|
|Ve|
h
VGSE (km/s)
Vex
Vey
Vez
i
VGSE (km/s)
Vix
Viy
Viz
j
T (eV)
Te||
Te⊥
Ti||
Ti⊥
k
Pa
Pplas_tot
nkTe
nkTi
P_B
Px_ram
26m50s
27m00s
27m10s
27m20s
27m30s
27m40s
2015/12/28 05h
Epoch

Figure 2

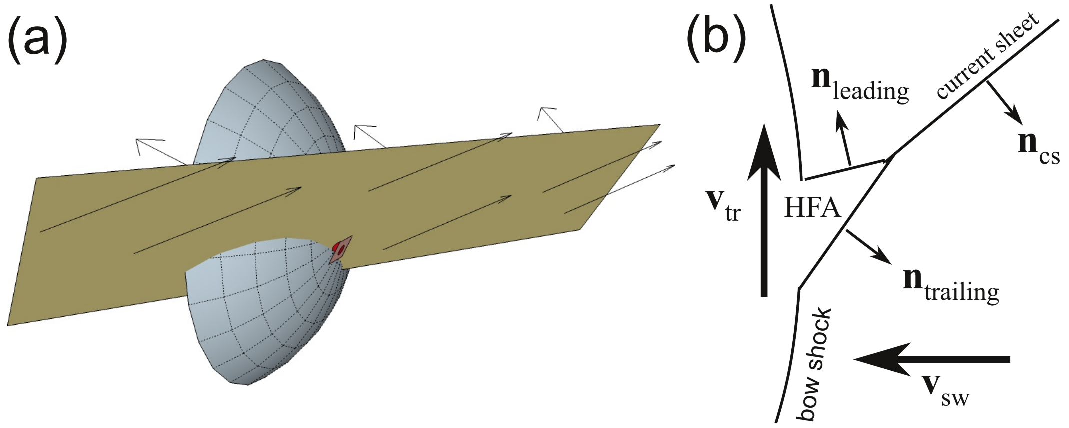
(a)
(b)
$\mathbf{n}_{\text{leading}}$
current sheet
$\mathbf{n}_{\text{cs}}$
$\mathbf{v}_{\text{tr}}$
HFA
$\mathbf{n}_{\text{trailing}}$
bow shock
$\mathbf{v}_{\text{sw}}$

Figure 3

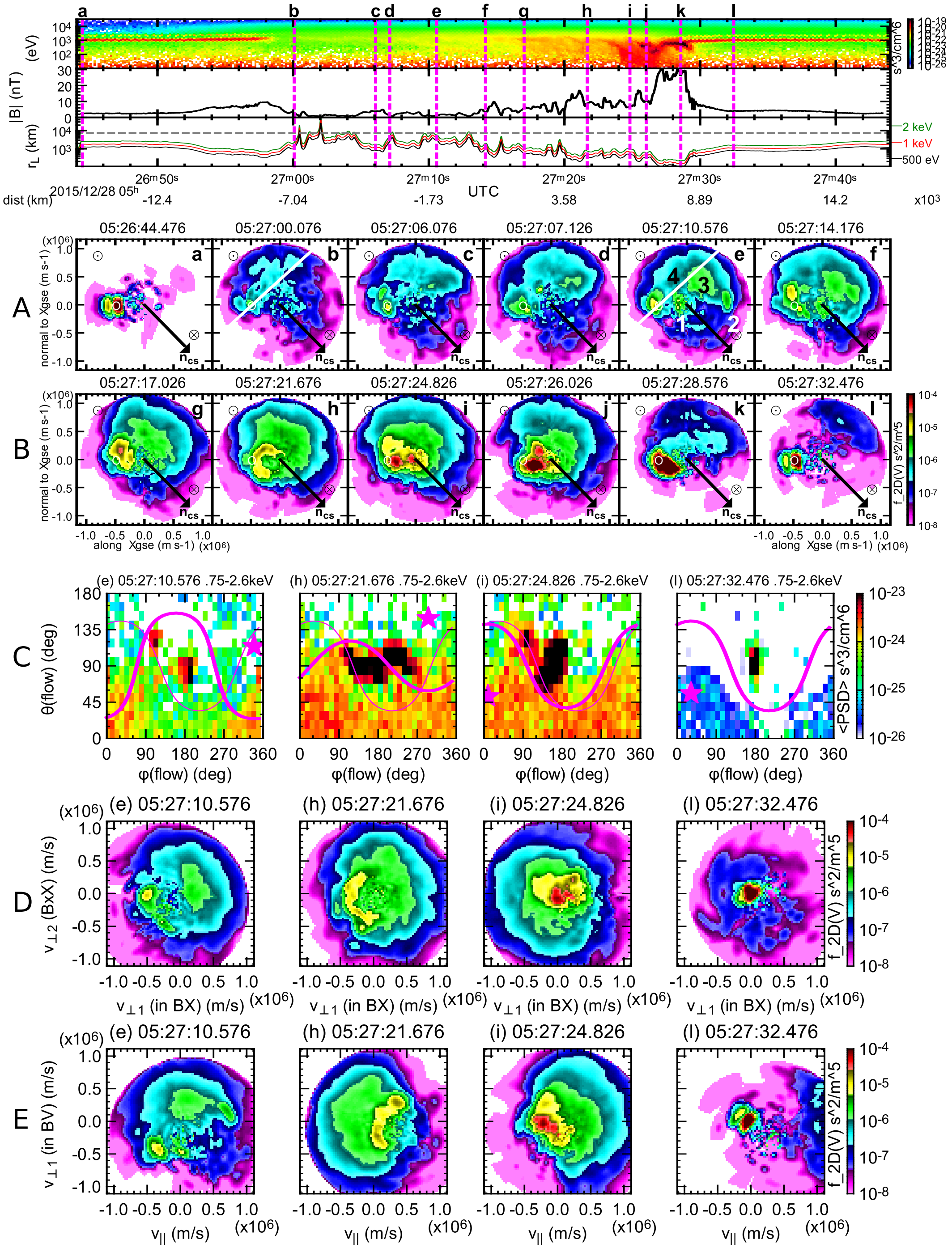
a b c d e f g h i j k l
(eV)
|B| (nT)
r_L (km)
2 keV
1 keV
500 eV
s^3/cm^6
2015/12/28 05h
26m50s 27m00s 27m10s 27m20s 27m30s 27m40s
UTC
dist (km) -12.4 -7.04 -1.73 3.58 8.89 14.2 x10^3
A
B
C
D
E
05:26:44.476
05:27:00.076
05:27:06.076
05:27:07.126
05:27:10.576
05:27:14.176
05:27:17.026
05:27:21.676
05:27:24.826
05:27:26.026
05:27:28.576
05:27:32.476
normal to Xgse (m s-1)
along Xgse (m s-1) (x10^6)
n_cs
1 2 3 4
f_2D(V) s^2/m^5
(e) 05:27:10.576 .75-2.6keV
(h) 05:27:21.676 .75-2.6keV
(i) 05:27:24.826 .75-2.6keV
(l) 05:27:32.476 .75-2.6keV
θ(flow) (deg)
φ(flow) (deg)
<PSD> s^3/cm^6
(e) 05:27:10.576
(h) 05:27:21.676
(i) 05:27:24.826
(l) 05:27:32.476
v⊥2 (BxX) (m/s)
v⊥1 (in BX) (m/s) (x10^6)
v⊥1 (in BV) (m/s)
v|| (m/s) (x10^6)